Sensors and Actuators B 183 (2013) 627–635

Contents lists available at SciVerse ScienceDirect

Sensors and Actuators B: Chemical

journal homepage: www.elsevier.com/locate/snb

A personal device for analyzing carbon dioxide in real time and real breath: Experimental investigation and computational simulation

Di Zhao[a,b], Dylan Miller[a,c], Dangdang Shao[a,d], Xiaojun Xian[a], Francis Tsow[a], Rodrigo A. Iglesias[a], Erica S. Forzani[a,b,*]

[a] Center for Bioelectronics and Biosensors, Biodesign Institute, Arizona State University, Tempe, AZ 85287-5801, United States
[b] Chemical Engineering Program, School of Engineering of Matter, Transport and Energy, Arizona State University, Tempe, AZ 85287-5801, United States
[c] Mechanical Engineering Program, School of Engineering of Matter, Transport and Energy, Arizona State University, Tempe, AZ 85287-5801, United States
[d] School of Electrical, Computer and Energy Engineering, Arizona State University, Tempe, AZ 85287-5801, United States

ARTICLE INFO

Article history:
Received 12 February 2013
Received in revised form 26 March 2013
Accepted 27 March 2013
Available online 17 April 2013

Keywords:
Breath CO_2 analysis
Colorimetric sensor
3D simulation
Mass transport
Heat transfer
Chemical reaction kinetics

ABSTRACT

The analysis of breath CO_2 provides valuable information of pulmonary and cardiovascular functions, and plays a crucial role in monitoring patients with respiratory problems. Developing portable sensors for real breath CO_2 analysis has been challenging because exhaled breath is hot, humid and turbulent. In this work, we have developed, modeled and tested a portable CO_2 sensor that can analyze end tidal CO_2 concentration in breath and in real time accurately. The key components of the sensor comprise a fluidic system for efficient breath sample delivery and a colorimetric detection integrated into the fluidic system. The modeling includes turbulent mass transport, heat transfer from the samples at body temperature to the device environment, and chemical reaction mechanisms, including multiple reactions pathways and diffusion of CO_2 in the sensing layer. Furthermore, the sensor has been tested and compared with a standard commercial CO_2 analyzer, and the results are in good agreement with those of the commercial analyzer, and with the modeling.

Published by Elsevier B.V.

1. Introduction

Among various chronic diseases, chronic obstructive pulmonary disease (COPD) and asthma are the leading concerns [1–5]. About 10 million Americans have been diagnosed with COPD and another ~20 million with asthma [5,6]. Breath carbon dioxide analysis is a well-known method that measures the breath CO_2 level, which is proportional to the partial pressure of CO_2 dissolved in blood [7–12]. The method is popular, effective and widely used to diagnose and evaluate the states of COPD and asthma, however, most of the current CO_2 equipment are based on infrared detection, which requires collecting breath samples with a pump, sample treatment to reduce interference from high breath humidity [13], and frequent calibration originated from signal drift. The high cost has also limited the use of current CO_2 equipment inside hospitals [14].

An alternative approach to measure CO_2 is based on colorimetric detection, which has been explored and developed by many groups with promising performance [15–20]. Nonetheless, in order to analyze CO_2 in real time and real breath (high humidity and temperature) without pre-conditioning of the sample, we need not only fast and accurate CO_2 sensor, but also efficient and reliable fluidic design that can deliver the breath sample from the mouth to the sensor, which remains unsolved in the existing colorimetric detections.

In the present work, we have successfully developed a low cost and high performance breath CO_2 analyzer for the personal use at home. The analyzer features an accurate colorimetric CO_2 sensor that can analyze end tidal CO_2 concentration in real time. More importantly, it includes a fluidic system designed for efficient delivery of breath sample to the colorimetric sensor. The integrated system, including both the sample delivery fluidics and CO_2 sensor, has been designed and optimized by carefully modeling and testing mass transport, heat transfer, and chemical reactions, such that we are able to achieve reliable analysis of real breath sample with high humidity and varying temperature. We believe that this integrated and system-level approach can be also applied to other types of chemical sensors for real breath analysis.

2. Experimental

2.1. Reagent and sensor preparation

The CO_2 colorimetric chemical sensor in the present work contained a HCO_3^-/CO_3^{2-} buffer and thymol blue as a color indicator

* Corresponding author at: Center for Bioelectronics and Biosensors, Biodesign Institute, Arizona State University, Tempe, AZ 85287-5801, United States.
Tel.: +1 480 965 9058; fax: +1 480 965 9457.
E-mail address: erica.forzani@asu.edu (E.S. Forzani).

0925-4005/$ – see front matter. Published by Elsevier B.V.
http://dx.doi.org/10.1016/j.snb.2013.03.138

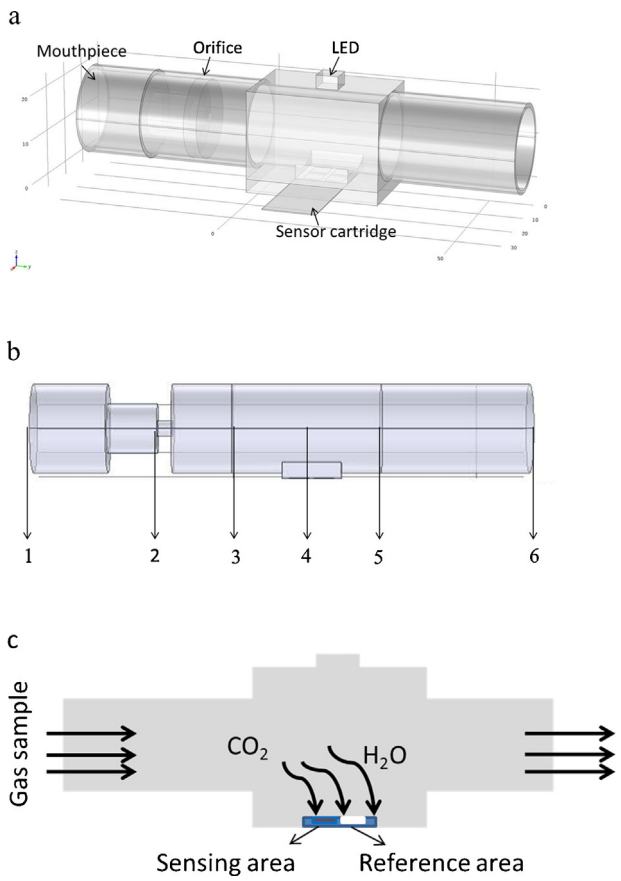

Fig. 1. (a) 3D geometry of the colorimetric CO_2 analyzer device and main device components. Simulated and real expired air was passed through the device from the mouthpiece. (b) Lateral view of the significant positions of the device indicated as follows: 1, inlet; 2, orifice (device narrowest portion); 3, middle portion between inlet and sensor chamber; 4, sensor chamber; 5, portion between sensor chamber and the outlet; 6, outlet. (c) Schematic representation of sample flow direction, and sensor cartridge components, showing the position of the sensing and reference areas.

[15–20]. All the reagents used in this work were analytical grade and purchased from Sigma-Aldrich (St. Louis, MO, USA). The sensor cartridge was made of a transparent plastic sheet, on which a sensing and reference areas were created (Fig. 1). The sensing area was coated with a solution containing HCO_3^-/CO_3^{2-} buffer and thymol blue, while the reference area was coated with HCO_3^-/CO_3^{2-} buffer only. The thicknesses of chemical coating layers for both the sensing and reference areas were determined to be a few hundreds of μm.

When the warm breath sample was brought into contact with the sensing cartridge, water vapor condensed on the sensor surface, forming a thin film of aqueous solution (see more details in later sections). Initially, the pH of the solution film was found to be ~9.05, but it decreased as CO_2 in the breath dissolved in the film. The pH decrease in the sensing area was detected by a color change of thymol blue from blue to yellow due to $pKa_2 \sim 8.0$–9.6 [15,16]. It is important to notice that the condensation of water plays role of hydrating the sensing chemicals and promoting the absorption of CO_2. In contrast, the reference area did not contain thymol blue dye and its color change was negligible, which served as a reference to correct drift in the color detection system.

2.2. Device description

The CO_2 analyzer is sketched in Fig. 1. It has a detection chamber, which includes a red LED (wavelength = 633 nm, LEDtronics. Inc., CA, USA) at the top of chamber as light source and a photodiode array (OSRM GmbH, Germany) at the bottom as light detector. The LED wavelength was chosen to closely match the absorption peak of Thymol Blue (615 nm). The detection chamber has also a sensor cartridge receiver located above the light detector. A sensor cartridge is inserted into the sensor cartridge receiver, and illuminated by the light source. The absorbance of the sensing area on the sensor cartridge is determined from the measured light intensities of the sensing and reference areas as a function of time, according to

$$Absorbance(t) = -\log_{10}\left(\frac{I_{sensing}(t)}{I_{reference}(t)}\right), \quad (1)$$

where $I_{sensing}$ and $I_{reference}$ are light intensities for the sensing and reference areas, respectively. Absorbance change is given by

$$\Delta Abs(t) = Absorbance(t) - Absorbance(0), \quad (2)$$

where $Absorbance(0)$ is the absorbance prior to the exposure of the sensor surface to breath sample. The measured absorbance change can be further normalized by the initial absorbance value, and it is the normalized absorbance change, Normalized $\Delta Abs(t)$, that is used to characterize the color change of thymol blue associated to CO_2 concentrations in the present work.

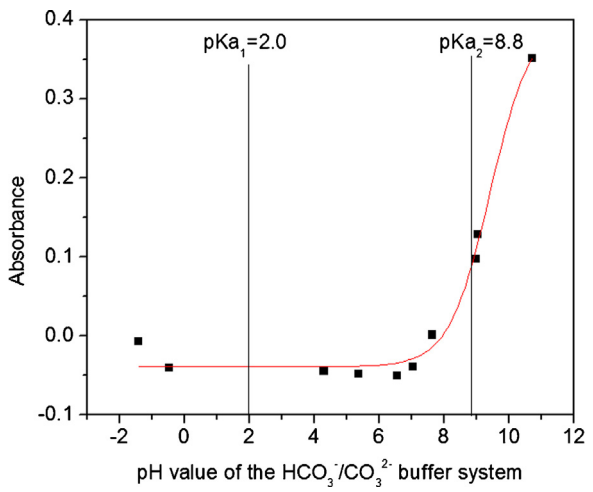

Fig. 2. The relationship between the measured normalized absorbance change and the pH of sensing HCO_3^-/CO_3^{2-} buffer system modified with thymol blue. The absorbance value increased with pH and followed a sigmoidal function: $Absorbance = 0.4 - \frac{0.4386}{1+\exp((pH-9.41085)/0.63016)}$. Values of p*K*a for thymol blue are indicated in the figure. Detected color changes in the CO_2 analyzer device were due to pKa_2 (with a color change from blue ($pH > pKa_2$) to yellow ($pH < pKa_2$)).

2.3. Device characterization – chemical characterization

Since the CO_2 detection is based on the pH change, which is measured from the color change, a calibration curve between absorbance change and the pH value is required, which was obtained by casting solutions of different pH values (measured with a pH electrode, Extech Instruments, NH, USA) onto the sensing area. The calibration curve, shown in Fig. 2, can be fit with a simple function,

$$Absorbance = 0.4 - \frac{0.4386}{1+\exp((pH-9.41085)/0.63016)}. \quad (3)$$

Using the calibration function by Eq. (3), one can relate the measured color change to the chemical reaction-induced pH change in the sensing area, which was needed for direct comparison between the measured color change and simulated chemical reaction taking place in the sensing area.

Table 1
Reynolds number (Re)[a] of the CO_2 analyzer device under different flow rate.

Flow rate (L/min)	6	8	10	12	14	16	18	20
Re	2697	3596	4495	5393	6292	7191	8090	8989

[a] $Re = \rho v D/\mu$, where ρ is the density of expired air (1.26 kg/m^3), v is the mean velocity of the flow, D is the diameter of the device (labeled as position 2 in Fig. 1b), μ is the dynamic viscosity of expired air (1.983×10^{-5} kg/m s).

Another important calibration is to determine the relationship between the color change and the breath CO_2 concentration, which can be achieved through two methods. In the first technique, we prepared artificial expired breath samples by mixing 80% N_2 + 20% O_2 gas with different concentrations of CO_2 (Praxair. Inc.), and then pumped (Aqueon, WI, USA) the mixed gases through a sealed water system immersed in a thermostatic water bath (Thermo Scientific, USA) at 35 °C to generate 35 °C and 100% relative humidity artificial breath. The CO_2 concentration tested in this system ranged from 0.03% to 6.5%. The artificial breath samples were introduced into the breath analyzer at a flow rate between 6 L/min and 18 L/min. In the second method, we directly used real breath samples from volunteers to further validate the performance of our breath analyzer.

2.4. Device characterization – temperature and flow characterization

During the tests, we have measured the temperature profile along the flow pathway for both the artificial and real breath samples by placing temperature probes at different positions in the CO_2 analyzer device. The flow rate and the pressure drop along the flow pathway were monitored with a flow meter (Newark, flow sensor 0–20 LPM) and a differential pressure sensor (All Sensors, USA).

3. Simulation methods

Numerical simulation of the CO_2 analyzer device was performed using the finite element method (Comsol Multiphysics COMSOL, Inc., MA, USA). The simulation included models for mass transport, heat transfer, and chemical reactions between the breath sample and the sensor surface. The 3D geometry of the flow path and detection chamber is shown in Fig. 1.

3.1. Mass transport and heat transfer simulation

To model the mass transport, the Reynolds numbers under various breathing conditions, e.g. flow rates between 6 and 20 L/min, were determined at the critical narrowest flow path of the system (position 2, Fig. 1b), which were relatively large (Table 1), indicating the presence of turbulent flow [21]. It is also worth to notice that the presence of a sharp orifice in the geometry of the system introduced a turbulent flow that not only affected position 2 (Fig. 1b) but also positions located downstream along the device (see below, Fig. 3a). For this reason, a turbulent flow model was used. In addition, since the pressure change across the analyzer is relatively small (<14 cm H_2O for 6–18 L/min), the breath sample was treated as incompressible gas in the model simulation.

The turbulent flow model used here is based on the Reynolds Averaged Navier-Stokes equation, which includes the turbulent kinetic energy (k) and turbulence dissipation rate (ε). This model is known as the $k-\varepsilon$ turbulence model, and takes the form of

$$\rho(\vec{u}\cdot\nabla)\vec{u} = \nabla[-p\vec{I} + (\mu+\mu_T)(\nabla\vec{u} + (\nabla\vec{u})^T) - \frac{2}{3}\rho\kappa\vec{I}] + \vec{F} \quad (4)$$

with $\mu_T = \rho C_\mu(\kappa^2/\varepsilon)$ and $\nabla\cdot(\rho\vec{u}) = 0$, where ρ is density of expired air (~1.26 kg/m^3), $\nabla\vec{u}$ is velocity gradient tensor, $(\nabla\vec{u})^T$ is

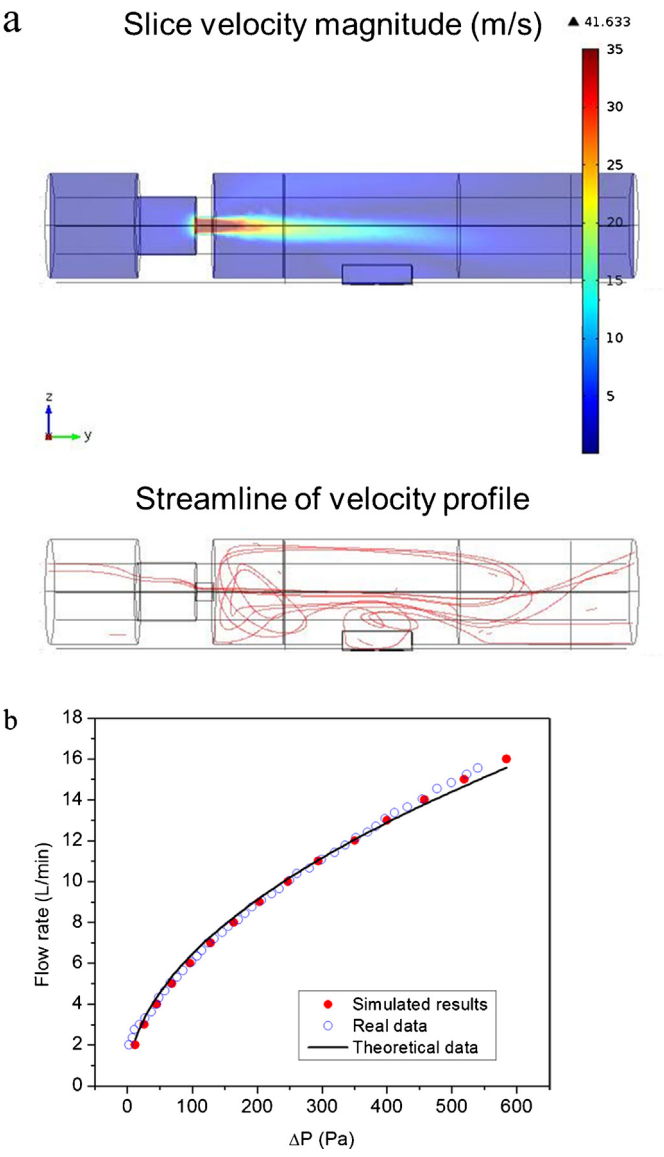

Fig. 3. Mass transport characterization of the CO_2 analyzer device: (a) velocity profile and streamline of velocity profile for 6 L/min flow rate. (b) The pressure drop of the airflow between position 5 and 2 (~1 mm away from orifice) at different flow rates. The experimental data (◯) fitted the theoretical results (solid line) obtained from Bernoulli's equation, and showed good agreement with the simulated data (●) from $k-\varepsilon$ turbulence model.

"transpose" of the velocity tensor, p is pressure, μ is dynamic viscosity of expired air, μ_T is turbulent viscosity, $\vec{F}$ is volume force, C_μ is a model constant (=0.09), and $\vec{u}$ is the average velocity [21].

In addition to considering turbulent flow, we took into account heat transfer between the relative warm breath (~35 °C) and the cold surroundings (~25 °C). Since the flow rate is rather fast (6–18 L/min), heat transfer due to conduction mechanism was assumed negligible, and mainly driven by forced convection, which is described by

$$-\vec{n}\cdot(-K\nabla T) = h\cdot(T_{ext} - T) \quad (5)$$

where $\vec{n}$ is the flow direction, K is the thermal conductivity of airflow, ∇T is temperature gradient tensor, h is the convection heat-transfer coefficient, T_{ext} is the device external temperature and T is the fluid temperature [21].

Eqs. (4) and (5) were solved numerically with the following boundary conditions.

1) Flow velocity on the device wall [21]:

$$\vec{u}\cdot\vec{n}=0 \tag{6}$$

$$\left[(\mu+\mu_T)(\nabla\vec{u}+(\nabla\vec{u})^T)-\frac{2}{3}\rho k\vec{I}\right]\vec{u}=-\rho\frac{u_\tau}{\delta_w^+}\vec{u}_{\tan g} \tag{7}$$

$$\vec{u}_{\tan g}=\vec{u}-(\vec{u}\cdot\vec{n})\vec{n} \tag{8}$$

$$\nabla k\vec{n}=0 \tag{9}$$

where $\vec{n}$ indicates the flow direction, and $\vec{u}_{\tan g}$ represents the tangential direction of the velocity vector.

2) Flow velocity at the device inlet:

$$\vec{u}=-U_0 f(t)\vec{n} \tag{10}$$

where U_0 is linear velocity of airflow at the inlet, $f(t)$ is a time dependent function, which can be used to describe the breath pattern (assumed constant in this work), and $\vec{n}$ is the flow direction.

$$\kappa=\frac{2}{3}(U_0\vec{I}_T)^2 \tag{11}$$

where I_T is turbulent intensity.

$$\varepsilon=C_\mu^{3/4}\frac{\kappa^{3/2}}{L_T} \tag{12}$$

where L_T is turbulence length scale.

$$\left[(\mu+\mu_T)(\nabla\vec{u}+(\nabla\vec{u})^T)-\frac{2}{3}\rho k\vec{I}\right]\vec{n}=0 \tag{13}$$

where the viscous stress $((\mu+\mu_T)(\nabla\vec{u}+(\nabla\vec{u})^T)\vec{n})$ and apparent stress $(-\frac{2}{3}\rho k\vec{I}\cdot\vec{n})$ were considered zero.

3) Flow velocity at the device outlet:

$$p_2=P_0=P_{atm} \tag{14}$$

$$\nabla k\vec{n}=0 \tag{15}$$

$$\nabla\varepsilon\vec{n}=0 \tag{16}$$

4) Temperature at the inlet:

$$T_{in}=306.80\,\mathrm{K} \tag{17}$$

5) Temperature on the wall and at the outlet:

$$T_w=298.15\,\mathrm{K} \tag{18}$$

3.2. Chemical reaction kinetics

As described in the Experimental Section, the measurement of CO_2 concentration was based on the absorption of CO_2 by the HCO_3^-/CO_3^{2-} buffer solution, which is formed due to surface modification and water condensation from the sample (see more details below). Therefore, the transformation and chemical reactions of CO_2 in the sensing and reference areas were described by

$$CO_2(g)\underset{k_0'}{\overset{k_0}{\rightleftarrows}}CO_2(aq) \tag{R1}$$

$$CO_2+H_2O\underset{k_1'}{\overset{k_1}{\rightleftarrows}}H_2CO_3 \tag{R2}$$

$$H_2CO_3\underset{k_2'}{\overset{k_2}{\rightleftarrows}}H^+ + HCO_3^- \tag{R3}$$

$$H^+ + OH^-\underset{k_3'}{\overset{k_3}{\rightleftarrows}}H_2O \tag{R4}$$

$$HCO_3^-\underset{k_4'}{\overset{k_4}{\rightleftarrows}}CO_3^{2-}+H^+ \tag{R5}$$

Steps 2–5 can be combined and simplified as

$$CO_2+OH^-\underset{k_5'}{\overset{k_5}{\rightleftarrows}}HCO_3^- \tag{R6}$$

$$CO_2+H_2O\underset{k_6'}{\overset{k_6}{\rightleftarrows}}H^+ + HCO_3^- \tag{R7}$$

where (R6) represents CO_2 reaction in the presence of excessive hydroxide anions, and (R7) represents CO_2 reaction after consumption of hydroxide anions. (R6) and (R7) were assumed to take place faster than (R1) because the latter includes dissolution and internal diffusion of CO_2 within the thin solution films formed by water vapor condensation. This assumption is reasonable because the acid-base reaction takes place in the pico-second range [22], compared to the milli-second range estimated for the diffusion of $CO_2(aq)$ within the thin film layer on the sensor cartridge.

Thymol blue (TB) was the indicator for $[H^+]$ and $[OH^-]$ resulted from steps (R6) and (R7), which are described by

$$TBH_2(\mathrm{red})+H_2O\underset{k_7'}{\overset{k_7}{\rightleftarrows}}TBH^-(\mathrm{yellow})H_3O^+ \tag{R8}$$

$$TBH^-(\mathrm{yellow})+OH^-\underset{k_8'}{\overset{k_8}{\rightleftarrows}}TB^{2-}(\mathrm{blue})+H_2O \tag{R9}$$

$$TB^{2-}(\mathrm{blue})+OH^+\underset{k_9'}{\overset{k_9}{\rightleftarrows}}TBH^-(\mathrm{yellow}) \tag{R10}$$

Note that steps (R8)–(R10) are also acid-based reactions, and can be combined with (R6) and (R7) to reflect the color changes due to the presence of dissolved $CO_2(aq)$ in the sensing area, which takes the form of,

$$TB^{2-}(\mathrm{blue})+H_2O+CO_2(aq)\rightleftarrows TBH^-(\mathrm{yellow})+OH^-+CO_2(aq)\rightleftarrows TBH^-(\mathrm{yellow})+HCO_3^- \tag{R11}$$

$$TBH^-(\mathrm{yellow})+CO_2+H_2O\rightleftarrows TBH^-(\mathrm{yellow})+H^++HCO_3^-\rightleftarrows TBH_2(\mathrm{red})+HCO_3^- \tag{R12}$$

Because the acid-base reactions and associated indicator reactions (steps (R2)–(R12)) are fast, the rate determining step is the dissolution and diffusion of CO_2 (step (R1)), which can be described by the rate equation,

$$\frac{d[CO_2]}{dt}=aC^*\sqrt{D(r+s)} \tag{19}$$

$$C^*=\frac{P_{CO_2}}{K_{CO_2}} \tag{20}$$

where a and s are constants, D is the diffusion coefficient of CO_2 ($\sim 1.42\times10^{-5}\,\mathrm{cm^2/s}$), P_{CO_2} is the partial pressure of CO_2, K_{CO_2} is Henry's constant of CO_2 (29.4 L atm/mol) and r is the apparent reaction constant given by

$$r\approx k_6+k_5\frac{K_w}{K_{a2}}\frac{[CO_3^{2-}]}{[HCO_3^-]} \tag{21}$$

where $(K_w/K_{a2})([CO_3^{2-}]/[HCO_3^-]) = [OH^-]$, $K_{a2} = ([H^+][CO_3^{2-}]/[HCO_3^-])$, and $K_w = [H^+][OH^-]$.

Note that the above equation of CO_2 diffusion rate, was cited from Danckwerts et al. under a similar condition [14,23].

Based on steps (R6) and (R7), the concentration of protons in the thin solution films of the sensing and reference areas is given by

$$[H^+] = \frac{K_{a1} \times [CO_2]}{[HCO_3^-]} \tag{22}$$

where $K_{a1} = 4.6 \times 10^{-7}$.

Based on Eq. (22), and the assumption that the concentration change of bicarbonate is negligible compared to the initial concentration ~0.01778 mol/L, the proton production rate can be expressed as

$$\frac{d[H^+]}{dt} = \frac{K_{a1}}{[HCO_3^-]} \times \frac{d[CO_2]}{dt}. \tag{23}$$

Eq. (23) and the related Eqs. (19)–(22) were used to correlate gas phase CO_2 concentration (P_{CO_2}) and absorbance changes due to $[H^+]$ changes, using the formerly introduced function in Fig. 2 (Eq. (3)). It is worth to notice that the transport of CO_2 through the sensing layer occurred on the perpendicular direction along the sensor surface. While the condensation of H_2O on the sensor surface was assumed to be instantaneous driven by the gradient difference between the sample temperature and the ambient temperature (which applies to the sensor surface), the absorption of CO_2 was governed by internal diffusion in the sensing layer (given by Eqs. (19) and (20)). Furthermore, the condensed H_2O was limited to a constant amount resulting from a constant sample volume passed through the system. These conditions defined a constant bicarbonate concentration for a given CO_2 concentration in the sample. As a result, the concentration of protons across the sensor surface could be simulated through a modified surface reactions model using Eq. (23) and the simulated absorbance patterns were obtained from Eq. (3) (see below). In addition to Eq. (3) and Eqs. (19)–(23), the mass transport and heat transfer equations (Eqs. (4) and (5)) were used to simulate the response of the sensor as a function of CO_2 concentrations ranging 0.03–6.5%, at 35 °C. These equations were also used to determine the effective surface density of protons (moles/cm^2) that was correlated to color changes on the sensor surface (see below).

4. Results and discussion

4.1. Characterization of the mass transport

In order to characterize the flow of the breath CO_2 sensor, mass transport simulations were carried out under various flow rates. Fig. 3a shows the velocity profile (upper panel) and streamline (lower panel) at a flow rate of 6 L/min. The profile is clearly non-homogeneous and turbulent, especially in the region where the orifice (shown as the narrowest diameter portion) is located, and near the sensor cartridge. This flow profile is different from the velocity profile expected for a flow path with a uniform cross sectional area [24].

As a method to validate the model simulation, volume flow rate vs. pressure difference across the orifice was measured experimentally. The result is compared with the simulation in Fig. 3b. Note that the pressure difference was determined by connecting the inlet and outlet of a differential pressure sensor at points 2 and 5 of the flow path (Fig. 1b). The experimental and simulated results are in quantitative agreement, indicating that the turbulent flow model provides accurate description of the fluidic dynamics of the system.

The simulation results were further validated as compared with the Bernoulli equation, which expressed the flow rate vs. pressure difference by

$$\text{Flow rate} = A_2 \cdot \sqrt{\frac{2}{(1-(A_2^2/A_1^2))}\left(\frac{\Delta P}{\rho}\right)}, \tag{24}$$

where ΔP is the pressure difference, ρ is the gas density, and A_1 and A_2 are the cross-sectional areas at the orifice and at a location behind the orifice, respectively. As shown in Fig. 3c, the flow rate – pressure difference relation by the Bernoulli principle agrees well with both the experimental and simulated results. It is worth to note that although the overall flow rate of the breath CO_2 sensor can be reasonably described by the Bernoulli principle, detailed velocity profile can only be obtained with the numerical simulation.

It is worth to notice that since there was an important agreement between experimental data and Bernoulli principle, Bernoulli equation was utilized to calibrate the pressure sensor used to measure flow rate in the CO_2 device. This fact allowed to establish the total volume of sample passed through the system via the integration of flow rate over time.

4.2. Characterization of the temperature profile

Simulations of heat transfer process were carried out to determine the temperature profile at different flow rates. Fig. 4a shows the temperature profile throughout the CO_2 sensor for a typical flow rate of 6 L/min. It can be observed that the temperature decreases from 35 °C at the inlet to ~28 °C at the outlet with an average temperature of 31 °C on the sensor cartridge. In addition, the heat loss was proportional to the flow velocity and the maximum temperature drop is across the narrowest portion of the device.

In order to corroborate the heat transfer model, the temperature was measured experimentally, and the results were compared to the simulations in Fig. 4b. It shows excellent agreement between the experimental and simulated temperature profiles. The temperature decreases along the flow path from the device inlet to the outlet. This temperature profile has an important implication in water condensation along the flow path and on the sensor cartridge based on the following consideration. Since the initial temperature of expired air is around 35 °C and the relative humidity of expired air is considered as constant (RH = 100%), the dew point of expired air reduced as the expired air was cooled down when it flows from the inlet towards the outlet of the device. As a result, water vapor condenses on the wall of the analyzer and on the sensor cartridge. As mentioned earlier, the detection mechanism of breath CO_2 originates from the chemical reactions of the dissolved CO_2 from the breath samples within the water condensation film formed on the sensor cartridge. Evidence of water condensation from the inlet and throughout the analyzer was gathered by using a Selected Ion Flow Tube-Mass Spectrometry (SIFT-MS), which allow determining in situ water vapor densities [25,26]. Accurate vapor densities readings were taken using the SIFT-MS (Profile 3 from Instrument Science) set with H_3O^+ ion source, and the instrument inlet tip. The readings ranged from breath condensing conditions (100% RH) at the inlet of the analyzer to ambient humidity (22% RH) at a distance of few centimeters away from the outlet. These evidences in connection to the observed water condensation on the sensor cartridge further allowed supporting the reaction mechanisms of the sensor.

4.3. Characterization of the chemical reaction

The basic sensing principle, as described earlier, is that the CO_2 in breath interacts with and thus decreases the pH of the sensing element, which is determined via monitoring the color change of thymol blue in the sensing area. The relationship between

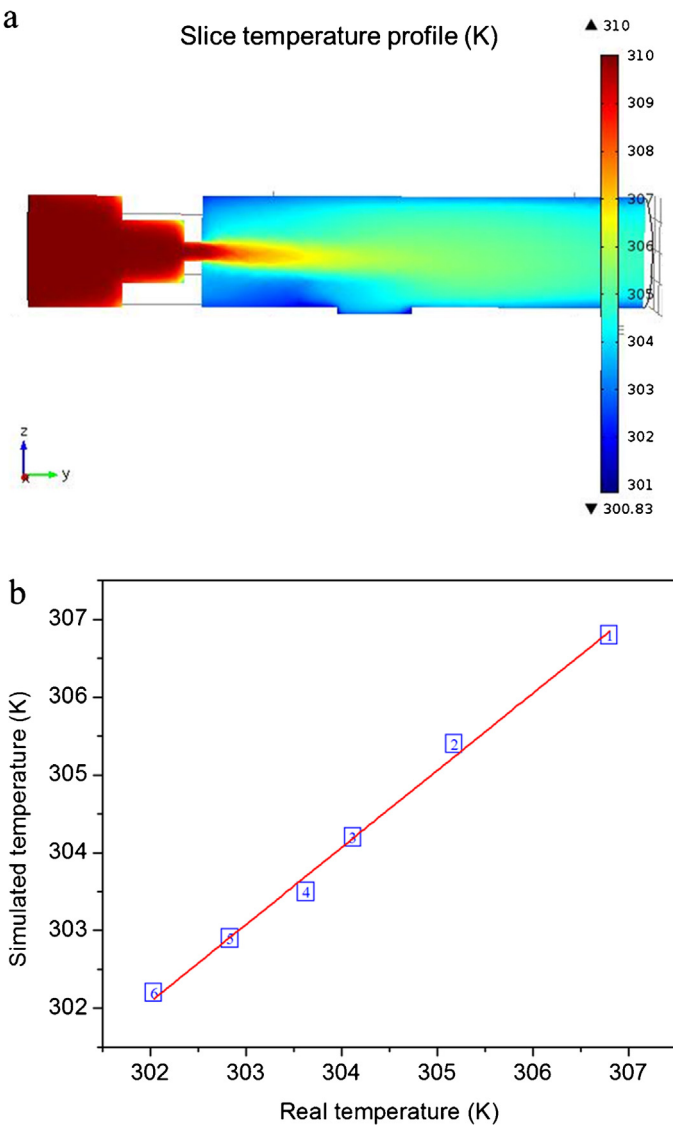

Fig. 4. Heat transfer characterization: (a) Temperature profile of the CO_2 analyzer device corresponding for a flow rate of 6 L/min with input and output temperature of 35 and 25 °C, respectively. (b) The temperature distribution of the artificial expired air throughout the device. There was a good correlation between real temperature (x) and the simulated temperature (y) with the following relationship: $y = 2.51 + 0.992x$, $r^2 = 0.9988$.

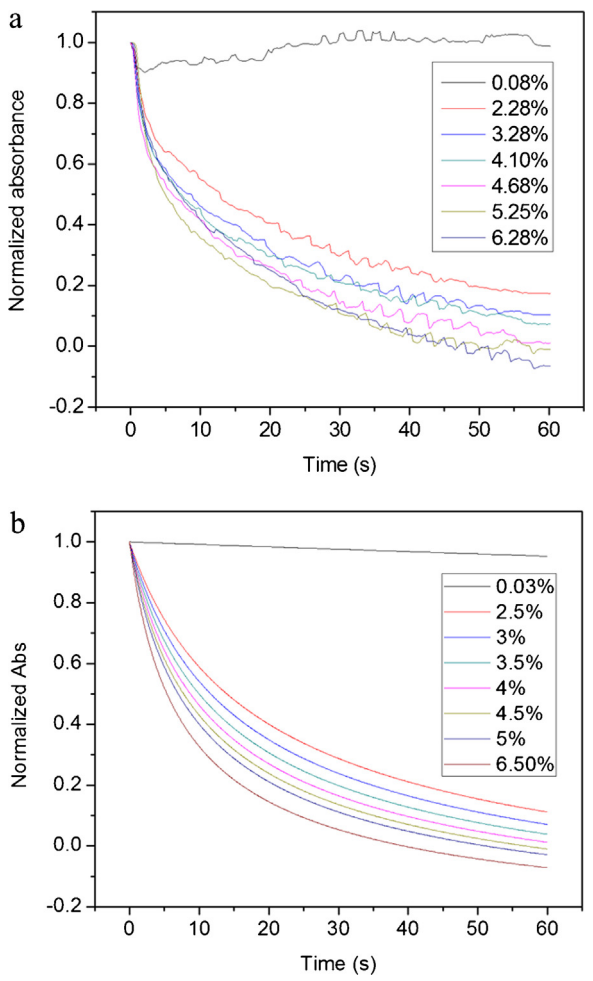

Fig. 5. (a) Measured and (b) simulated normalized absorbance vs. time at the CO_2 concentration of 0.03–6.50%, respectively. The normalized absorbance value decreased as thymol blue changed color from blue to yellow. (c) Calibration of sensor response to CO_2. The experimental data (■) are in good agreement with the simulated results (●). The Normalized ΔAbs decreased exponentially with the increasing concentration of CO_2 following the relationship: Normalized $\Delta Abs = 0.9941 \exp(-CO_2\%/1.46581) - 1.047$.

the concentration of CO_2 and the absorbance of thymol blue was investigated by both numerical simulation and experimental measurement.

Fig. 5a and b shows the measured and simulated normalized absorbance vs. time at the CO_2 concentration of 0.03% and 6.5%, respectively. First, the plots show that the simulated and experimental results are in good agreement, further validating the models used in the simulation. Second, the results show that the color change (of thymol blue from blue to green) at a fixed flow rate of 6 L/min takes place rapidly at the initial stage and then slows down. The rapid response in the early stage is due to reaction step (R6), which corresponds to the reaction of CO_2 with the excess amount of hydroxyl ions. Over time, hydroxyl ions are consumed and step (R7), corresponding to the dissolution of CO_2, takes over, which is denoted by the slower phase at a later stage.

Furthermore, we are able to correlate the maximum color change (or maximum absorbance change) to the CO_2 concentration. Fig. 5c plots experimental and simulated maximum changes in the normalized absorbance vs. CO_2 concentration, and the good agreement indicates that our proposed reaction mechanism and kinetics are reasonable.

We also would like point out that the chemical reaction of the CO_2 analyzer was the spatial distribution of the color change across the sensor surface. Non-uniform distribution of the color change is expected because the flow is inhomogeneous and turbulent, which affects the pH or proton profile across the sensor surface, resulting in inhomogeneous color development. Consequently, the spatial distribution of the color change may be used to characterize the actual concentration gradient of protons on the sensor surface. Fig. 6a and b shows an experimental image of the sensing area after 6.5 s of exposure to a CO_2 sample, and a simulated image obtained under a similar condition, respectively. Note that the simulated image from the simulated proton concentration profile is shown in Fig. 5d, which also matched the proton distribution pattern calculated from the real image (Fig. 5c). The simulation not only reproduces the inhomogeneous color change across the sensor surface, but also predicts the reaction time necessary for the accurate CO_2 concentration analysis in the sample. For instance, relatively short exposure (6.5 s) of the sensor surface to CO_2 concentrations that are relevant to real breath samples produced non-homogeneous color development at the top left

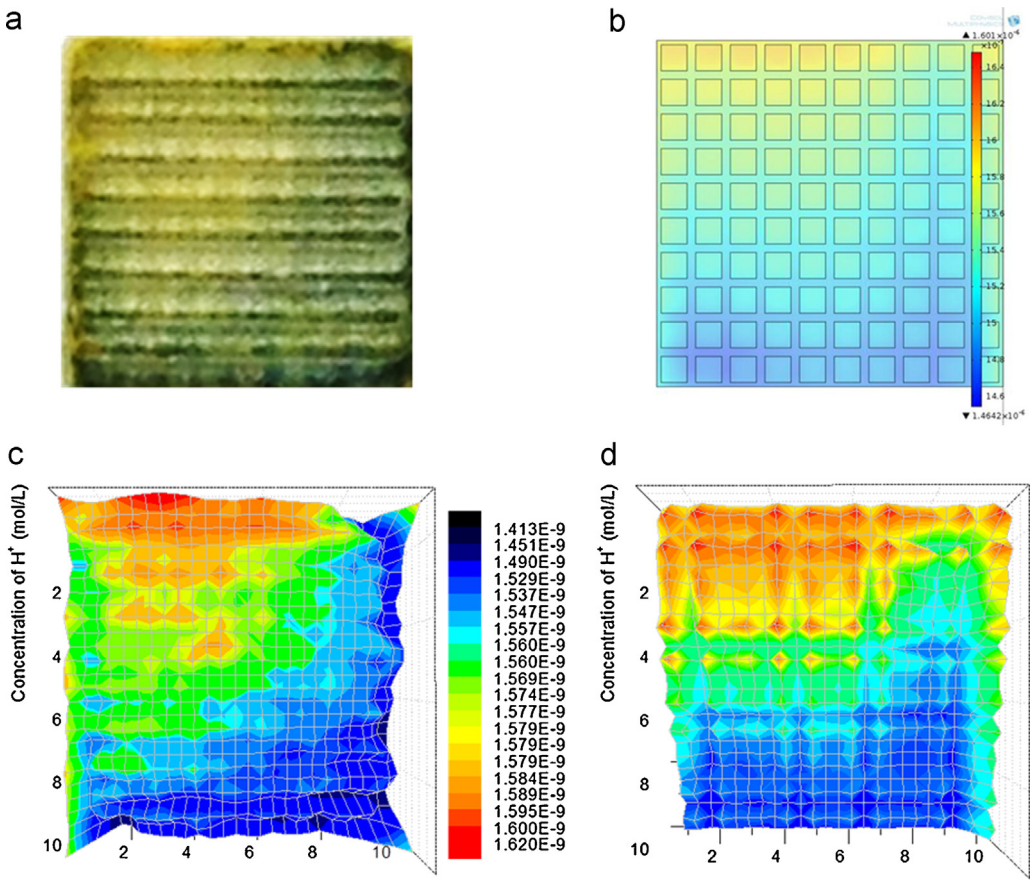

Fig. 6. (a) The real and (b) simulated sensing area at $t = 6.5$ s. The simulated sensing surface represented the concentration gradient of protons. (c) The 3D surface plot of proton concentration in the real sensing area and (d) the 3D surface plot of proton concentration in the simulated sensing area. The concentration distribution of protons was non-uniform across the sensing area.

part of the sensing area (yellow), while the other areas remain blue. Therefore, sufficient exposure time is needed to minimize the inhomogeneity caused by turbulent flow, and to ensure the reaction sites across the entire sensing area to react with CO_2 in the sample. Finally, the experimental and simulated images are in good agreement, which, once again, validates the models.

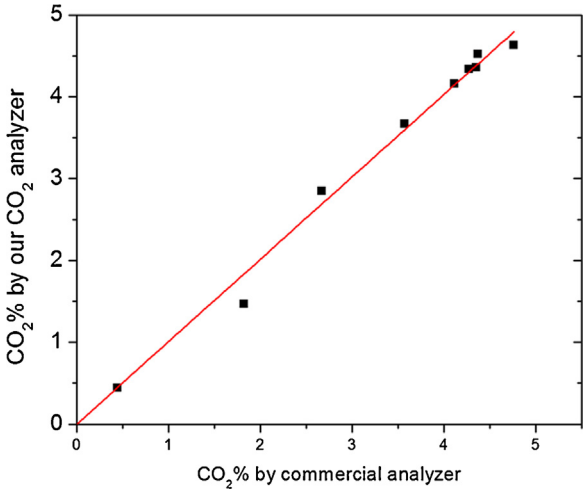

Fig. 7. Correlation of CO_2 levels from real and artificial breath samples determined by the CO_2 analyzer device (y) and a commercial CO_2 analyzer instrument (x). Linear correlation analysis of the variables was: $y = 1.007\,x$, $r^2 = 0.9981$ indicating good accuracy level.

4.4. Validation of the model

Based on the simulation and real image processing outcomes, we set a reaction time of 60 s for the CO_2 analyzer device, which is equivalent to 6 L sample volume for a typical breathing rate of 6 L/min. Therefore, 6 L volume samples of both real and artificial breath were used for the CO_2 analyzer device calibration. Once the breath CO_2 analyzer was calibrated, 6 L-volume samples were injected and processed as unknown samples using the device calibration to assess the CO_2 concentration. In parallel, a commercial CO_2 analyzer (Vacumed, Venture, CA) was used to determine the CO_2 concentration in the samples. In Fig. 7, we compare the results assessed from our CO_2 analyzer device and the commercial CO_2 analyzer. Clearly, the CO_2 concentration in both cases correlate at a slope of 1.01, an error of <2%, and a squared – regression coefficient (r^2) of 0.9981, which indicates an accuracy level close to a 100% between these two devices.

5. Conclusions

We have designed a colorimetic-based breath analyzer including a CO_2 sensor and a fluidic system for efficient delivery of high humidity and variable temperature breath sample, and have applied this analyzer to accurately detect and analyze the CO_2 in real breath and in real time. Moreover, we have proposed models taking into account mass transport, heat transfer and chemical reactions. The numerical simulation results based on the models and actual geometry of the device are compared with experimental

data, showing quantitative agreement. In addition, the simulations provide both spatial and temporal distributions of breath flow velocity, pressure and temperature, and also spatial profiles color development over time. This information is difficult to achieve merely from experiments, but is critical for optimizing the performance of breath analyzer. Based on our experimental data and numerical simulation, we then developed a pocket-sized CO_2 breath analyzer with comparable performance to the bulky traditional CO_2 analyzer. With our pocket-sized analyzer, the patients with COPD and Asthma can easily test their CO_2 level and access their disease status at home. We emphasize that the idea of integrating breath sample collection, delivery and sensing, and the simulations that takes into account mass transport, heat transfer and chemical reactions should be applicable to other types of breath analyzers.

Competing interest

The authors declare no competing financial interest.

Author contributions

DZ optimized the CO_2 sensor cartridge development and calibration, and performed the computational simulation and experimental validation. XX developed new methods for reproducible mass production of sensor cartridges. DM developed the hardware for sensor cartridge holder and optical and flow components of the new device. FT ensured the quality of optoelectronic components of the new device. RI performed the spectroscopic analysis of the CO_2 sensor. DS measured the pressure drop at different gas flow rate and participated in imaging data processing. EF supervised the project.

Acknowledgements

This work was supported by National Institutes of Health, NIBIB 1R21EB014219. The authors acknowledge the support of Program Director, Dr. Brenda Korte, and N.J. Tao for technical support and discussions.

References

[1] S. Richardson, FOCUS: Journal for Respiratory Care and Sleep Medicine 6 (2006) 17–20.
[2] Centers for Disease Control and Prevention Home Page. http://www.cdc.gov/copd/ (accessed 17.11.11).
[3] N.S. Gooneratne, N.P. Patel, A. Corcoran, Chronic obstructive pulmonary disease diagnosis and management in older adults, Journal of the American Geriatrics Society 58 (2010) 1153–1162.
[4] Medical News Today Home Page. http://www.medicalnewstoday.com/articles/14222.php (accessed 30.10.04).
[5] Health Central Home Page. http://www.healthcentral.com/asthma/introduction-000004_4-145.html (accessed 03.05.11).
[6] D.M. Mannino, D.M. Homa, L.J. Akinbami, E.S. Ford, S.C. Redd, Chronic Obstructive Pulmonary Disease Surveillance – United States, 1971–2000, 2002. Centers for Disease Control and Prevention. http://www.cdc.gov/mmwr/preview/mmwrhtml/ss5106a1.htm (accessed 19.07.02).
[7] B.S. Kodali, Capnography in 911, 2008. Capnography Home Page. http://www.capnography.com/outside/911.htm (accessed 28.08.08).
[8] M.S. Raheem, O.M. Wahba, A nasal catheter for measurement of end-tidal carbon dioxide in spontaneously breathing patients: a preliminary evaluation, Anesthesia and Analgesia 110 (2010) 1039–1042.
[9] O.K. Kurt, S. Alpar, T. Sipit, S.F. Guven, H. Erturk, M.K. Demirel, M. Korkmaz, M. Hayran, B. Kurt, Diagnostic role of capnography in pulmonary embolism, American Journal of Emergency Medicine 28 (2010) 460–465.
[10] G. Cacho, J.L. Pérez-Calle, A. Barbado, J.L. Lledó, R. Ojea, C.M. Fernández-Rodríguez, Capnography is superior to pulse oximetry for the detection of respiratory depression during colonoscopy, Revista Espanola de Enfermedades Digestivas 102 (2010) 86–89.
[11] N.H. Ab-Rahman, T.A. Howe, A comparison of capnographic waveform indices and peak flow meter in the monitoring of asthmatic patients in emergency departments, Annals of Emergency Medicine 51 (2008) 476–477.
[12] F. Yanagidate, S. Dohi, Modified nasal cannula for simultaneous oxygen delivery and end-tidal CO_2 monitoring during spontaneous breathing, European Journal of Anaesthesiology 23 (2006) 257–260.
[13] B.S. Kodali, Physical Method of CO_2 Measurement, 2008. Capnography Home Page. http://www.capnography.com/new/index.php?option=com_content&view=article&id=216&Itemid=87 (accessed 27.08.08).
[14] P.V. Danckwerts, D. Roberts, Kinetics of CO_2 absorption in alkaline solutions—II: Absorption in a packed column and tests of surface-renewal models, Chemical Engineering Science 18 (1963) 63–72.
[15] N. Nakamura, Y. Amao, Optical sensor for carbon dioxide combining colorimetric change of a pH indicator and a reference luminescent dye, Analytical and Bioanalytical Chemistry 376 (2003) 642–646.
[16] S. Hiroyo, O. Eiji, A. Yasuhiko, Y. Kazuaki, Sensitivity of fiber-optic carbon dioxide sensors utilizing indicator dye, Sensors and Actuators B: Chemical 94 (2003) 276–281.
[17] M.S. Borisov, C.M. Waldhier, I. Klimant, S.O. Wolfbeis, Optical carbon dioxide sensors based on silicone-encapsulated room-temperature ionic liquids, Chemistry of Materials 19 (2007) 6187–6194.
[18] J.F. Fernández-Sáncheza, R. Cannas, S. Spichiger, R. Steiger, U.E. Spichiger-Keller, Optical CO_2-sensing layers for clinical application based on pH-sensitive indicators incorporated into nanoscopic metal-oxide supports, Sensors and Actuators B: Chemical 128 (2007) 145–153.
[19] M.A. Carvajal, I.M. Pérez de Vargas-Sansalvador, A.J. Palma, M.D. Fernández-Ramos, L.F. Capitán-Vallvey, Hand-held optical instrument for CO_2 in gas phase based on sensing film coating optoelectronic elements, Sensors and Actuators B: Chemical 144 (2010) 232–238.
[20] A. Mills, A. Lepre, L. Wild, Breath-by-breath measurement of carbon dioxide using a plastic film optical sensor, Sensors and Actuators B: Chemical 39 (1997) 419–425.
[21] R.B. Bird, W.E. Stewart, E.N. Lightfoot, Transport Phenomena, 2nd ed., John Wiley & Sons, New York, 2001.
[22] M. Rini, D. Pines, B. Magnes, E. Pines, E. Nibbering, Bimodal proton transfer in acid–base reactions in water, Journal of Chemical Physics 121 (2004) 9593–9610.
[23] P.V. Danckwwts, A.M. Kennedy, D. Roberts, Kinetics of CO_2 absorption in alkaline solutions—I Transient absorption rates and catalysis by arsenite, Chemical Engineering Science 17 (1962) 961–969.
[24] R. Wang, A. Prabhakar, R.A. Iglesias, X. Xian, X. Shan, F. Tsow, E.S. Forzani, N. Tao, A microfluidic-colorimetric sensor for continuous monitoring of reactive environmental chemicals, Sensors Journal IEEE 12 (2012) 1529–1535.
[25] P. Spanel, D. Smith, On-line measurement of the absolute humidity of air, breath and liquid headspace samples by selected ion flow tube mass spectrometry, Rapid Communications in Mass Spectrometry 15 (2001) 563–569.
[26] P.R. Boshier, J.R. Cushnir, V. Mistry, A. Knaggs, P. Španěl, D. Smith, G.B. Hanna, On-line, real time monitoring of exhaled trace gases by SIFT-MS in the perioperative setting: a feasibility study, Analyst 136 (2011) 3233–3237.

Biographies

Di Zhao received her BS and MS degree in Materials Science and Engineering from Tongji University in 2006 and 2009, respectively. She is currently working towards her Ph. D in Chemical Engineering at Arizona State University under the supervision of Dr. Erica Forzani. Her research interests focus on novel colorimetric sensors for the detection of gas and biomarkers in human breath.

Dylan Miller is a Graduate Research Assistant in the Center for Bioelectronics and Biosensors, The Biodesign Institute, at ASU. He completed his B.S. in Mechanical Engineering through Barrett, the Honors College at Arizona State University in May 2012 and joined the research team in BB center in the summer of 2010. Dylan is currently studying for his M.S. in Mechanical Engineering and plans to graduate in May 2013. His current research is focused on the mechanical design of wireless sensor devices with applications in mobile health and environmental safety.

Dangdang Shao is a PhD student in Electrical Engineering at ASU. She also works as Graduate Research Assistant in the Center for Bioelectronics and Biosensors, The Biodesign Institute. She completed her B.S. and M.S. at Shanghai Jiaotong University, China. She joined the research team in BB center in the summer of 2011. Her current research is focused on image processing for physiological signal detection.

Xiaojun Xian is Assistant Research Scientist of Center for Bioelectronics and Biosensors, The Biodesign Institute, at ASU. He received his PhD and BS in Physical Chemistry in Peking University, China. He joined Arizona State University in 2009 as Postdoctoral Research Associate and then worked as Assistant Research Scientist. His current research interests include development of mobile health sensor for chronic diseases management and environmental chemical sensor for personal exposure assessment.

Francis Tsow is Assistant Research Professor of the Center of Bioelectronics and Biosensors, the Biodesign Institute, at Arizona State University (ASU). He received his PhD in Electrical Engineering at Arizona State University. His current research focus on novel science and technology particularly those related to sensing applications.

Erica Forzani is Assistant Professor of the School for Engineering of Matter, Transport, and Energy, Ira A Fulton Schools of Engineering at Arizona State University (ASU); and Deputy Director of Center for Bioelectronics and Biosensors, at he Biodesign Institute, ASU. She received her PhD in Chemistry and BS in Clinical Chemistry and Biochemistry in Cordoba National University, Argentina. She joined Arizona State University in 2003 as research associate of the Department of Electrical Engineering, where she later worked as Assistant Research Professor. Her current research is focused on science and technology of novel sensors and integration of sensors into wireless, non-invasive and inexpensive sensor devices with applications in mobile health, and environmental health & safety.